SLAC-PUB-16540

Spatially resolved density and ionization measurements of shocked foams using x-ray fluorescence

M. J. MacDonald,[1,2,*] P. A. Keiter,[3] D. S. Montgomery,[4] H. A. Scott,[5] M. M. Biener,[5] J. R. Fein,[3] K. B. Fournier,[5] E. J. Gamboa,[2] G. E. Kemp,[5] S. R. Klein,[3] C. C. Kuranz,[3] H. J. LeFevre,[3] M. J.-E. Manuel,[3] W. C. Wan,[3] and R. P. Drake[3]

[1] *Applied Physics Program, University of Michigan, Ann Arbor, Michigan 48109, USA*
[2] *SLAC National Accelerator Laboratory, Menlo Park, CA 94025, USA*
[3] *Climate and Space Sciences and Engineering, University of Michigan, Ann Arbor, Michigan 48109, USA*
[4] *Los Alamos National Laboratory, Los Alamos, NM 87545, USA*
[5] *Lawrence Livermore National Laboratory, Livermore, CA 94550, USA*

(Dated: May 27, 2016)

We present experiments at the Trident laser facility demonstrating the use of x-ray fluorescence (XRF) to simultaneously measure density, ionization state populations, and electron temperature in shocked foams. An imaging x-ray spectrometer was used to obtain spatially-resolved measurements of Ti K-α emission. Density profiles were measured from K-α intensity. Ti ionization state distributions and electron temperatures were inferred by fitting K-α spectra to spectra from CRETIN simulations. This work shows that XRF provides a powerful tool to complement other diagnostics to make equation of state measurements in the warm dense matter regime.

I. INTRODUCTION

Warm dense matter (WDM) is a state of matter near solid densities and temperatures on the order of a few eV, which is too hot to be described by condensed matter physics and too strongly coupled to be considered an ideal plasma. A detailed understanding of the equation of state (EOS) of materials in the WDM regime is critical in modeling planetary interiors[1] and inertial confinement fusion implosions.[2]

Low density foams are an attractive material for scaled laboratory astrophysics[3] experiments because they can be produced in a wide range of densities. Hydrodynamic instabilities in shocked foams have been studied by imaging density fluctuations and material interfaces using x-ray radiography.[4] EOS measurements of shocked foams have been made using spectrally resolved x-ray scattering,[5] velocity interferometry,[6,7] and streaked optical pyrometry.[7] Here we present a technique to simultaneously measure density profiles and EOS variables with high brightness using x-ray fluorescence (XRF).

XRF is capable of measuring material properties in a wide range of conditions, ranging from chemical properties at ambient conditions[8] to experiments at high energy density (HED). In the context of HED experiments, imaging of XRF was first proposed to diagnose hydrodynamic experiments at large scale laser facilities.[9] It was subsequently demonstrated using a pinhole imaging system,[10] and more recently to infer fast electron transport in fast-ignition targets.[11] Spectral analysis of XRF has been used to measure radiative heating[12] and infer temperatures of metals directly irradiated by high-intensity short-pulse lasers.[13–17] In the present experiment we combine these useful aspects of XRF to simultaneously measure density, ionization state distributions, and electron temperatures in shocked foams.

XRF has several advantages compared to scattering techniques. First, XRF provides significantly higher signal levels than scattering measurements, as x-ray interaction cross sections are dominated by photoelectric absorption in the few to tens of keV energy range, as shown for Ti in Fig. 1. Additionally, XRF involves two photon energies: a probe x-ray source to produce electron vacancies and the resulting x-ray fluorescence. The probe x-ray energy is above the atomic absorption edge being probed, and is readily absorbed by the target material. Meanwhile, the x-ray fluorescence energy is below the absorption edge and easily escapes the target. The significant difference in attenuation for the probe and fluorescence x-ray energies is shown in the inset of Fig. 1, where the two energies used in this experiment are shown with vertical dashed lines (V He-α at 5.2 keV and Ti K-α

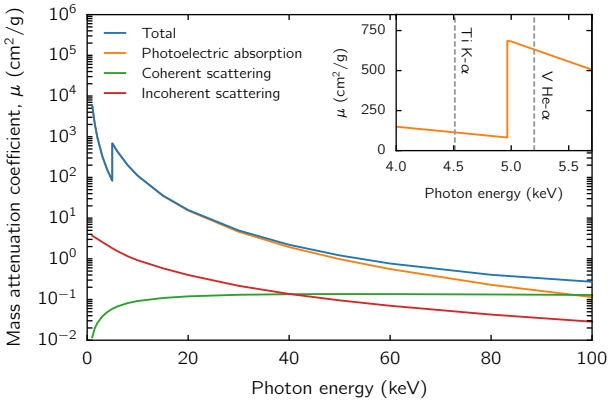

FIG. 1. Photon cross sections for Ti calculated using XCOM.[18] The total cross section is dominated by photoelectric absorption for photon energies below $\approx$ 80 keV. The inset shows the photoelectric absorption cross section for Ti at the probe energy (V He-α, 5.2 keV) and the fluorescence energy (Ti K-α, 4.5 keV).

This material is based upon work supported by the U.S. Department of Energy, Office of Science, Office of Basic Energy Sciences, under Contract No. DE-AC02-76SF00515, NSF and FES.

at 4.5 keV, respectively).

Secondly, XRF spectra are not sensitive to small variations in the probe spectrum. Unlike x-ray Thomson scattering (XRTS),[19] where the energy of scattered x-rays is measured relative to the incident energy, XRF energies depend only on the energy of atomic transitions. This property of XRF allows for a wider range of probe sources and does not require sources with narrow spectral bandwidths.

Here we present experiments conducted at the Trident laser facility[20] at Los Alamos National Laboratory (LANL) demonstrating the use of XRF to directly measure ion density profiles in shocked aerogel foams. XRF spectra are compared to CRETIN[21] simulations to infer ionization state populations and electron temperature.

II. THEORY

X-ray fluorescence from mid-Z elements is the result of radiative decay of an atom with an inner-shell electron vacancy. These vacancies can be created by exposing the material to a flux of particles with energies greater than the binding energy of the shell of interest, which interact with the bound electron and remove it from the atom.

Inner shell vacancies can be filled via a number of mechanisms including Auger decay, radiative decay, collisional transitions, or direct recombination. XRF is the result of radiative decay, where a photon is emitted with the energy of the electronic transition, such as K-α, K-β, L-α, etc. In this study K-shell vacancies in Ti were created using a V He-α x-ray source at 5.2 keV, above the Ti K-edge at 4.966 keV, and Ti K-α emission was measured. The Ti K-α doublet energies are 4.505 and 4.511 keV. The probability of radiative decay for each element is tabulated in the literature.[22] For Ti with a K-shell vacancy the probability of K-α emission is 0.17.

The K-α line emission energies depend on the electronic configuration of the atom. When the atom is ionized the screening of the inner electron orbitals is affected, the K-α energy is changed. K-α energies are tabulated for neutral and highly ionized states, such as the He-like and H-like states.[23] The K-α emission from these states are generally referred to as He-α and H-α x-rays, respectively. For intermediate ionization states an enormous number of possible electron configurations exist, leading to broadened K-α emission from contributions of the various configurations for a given charge state.

III. EXPERIMENTAL SETUP

In this experiment, shown schematically in Fig. 2, a 1 ns, 220 J beam at 2ω (527 nm) from the Trident laser system drove a shock in a cylindrical foam target, compressing and heating the foam. The laser was focused, using a random phase plate (RPP), to a 600 μm spot on a 6-μm-thick Mylar ablator on the drive side of the target. The ablator prevented direct irradiation of the low density foam. The foam targets were 2000 μm in length and 940 μm in diameter, inside a polyimide tube with a 53 μm wall thickness. A 5 μm V foil 1.0 mm from the foam on the side opposite of the drive was irradiated by a 1 ns, 180 J, 527 nm laser beam focused to 150 μm using a RPP, in order to produce a bright He-α x-ray source.

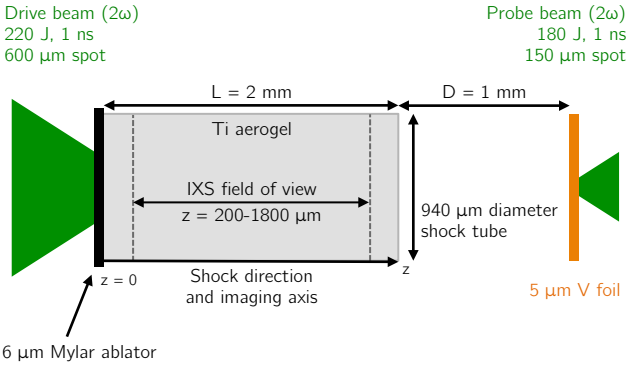

FIG. 2. Schematic of the targets used in this experiment. The drive beam irradiated a Mylar ablator to drive a shock in the Ti aerogel foam. The probe beam irradiated a V foil to produce He-α x-rays at 5.2 keV. The IXS provided spatially resolved spectral measurements of Ti K-α emission along the axis of the shock tube.

The primary diagnostic on the experiment was an imaging x-ray spectrometer (IXS),[24] which provided spatially resolved spectra resolved along the axis of the shock tube. This diagnostic used a toroidally bent Ge(400) crystal with radii of curvature of 400 and 200 mm in the spectral and imaging directions, respectively. The crystal was placed 139.9 mm from target chamber center. X-rays were detected using Fuji BAS-SR image plate placed 388.8 mm from the crystal, satisfying the imaging condition for the crystal optic with a magnification of 2.78 centered at the Ti K-α energy of 4.5 keV.

The spectral dispersion of the IXS was calibrated using the Ti K-α doublet. The spectral resolution of 2.1 eV was calculated by fitting a Voigt profile to the Ti K-α doublet produced by unshocked material. The spatial resolution of 70 μm was measured using Au grids with 35 μm bar thickness and 125 μm pitch, backlit by line emission from laser-irradiated Sc foils. Spatial profiles measured using these grids were fit using a Gaussian instrument function to determine the spatial resolution of the detector. The temporal resolution in this experiment was limited by the 1 ns duration of the probe x-rays, resulting in 70 μm of motion blurring.

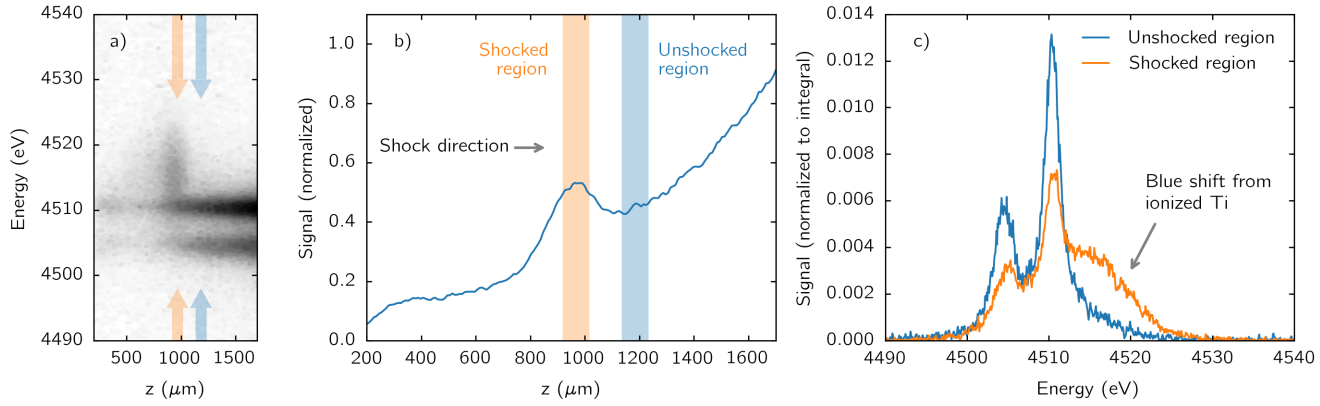

FIG. 3. a) Raw image plate data from the IXS showing the shifted spectrum at the shock interface, b) the spatial line out summing over spectral components at t = 15 ns, and c) the spectral data for the two regions highlighted in the spatial line out showing the shifted K-α fluorescence in the shocked foam as compared to the Ti in the unshocked foam.

A. Ti doped aerogel foams

Ti doped aerogel foams were chosen for this experiment because of their low material density and high atomic fraction of Ti. The aerogel foam consisted of SiO_2 scaffolding with an average distance between ligaments on the order of one micron coated with TiO_2,[25] providing a uniform concentration of Ti on a scale much smaller than the spatial resolution of the detector. This made it possible to directly correlate the XRF intensity to material density.

The low density of these foams enabled temperatures in the post-shock material to be high enough to observe shifts in the Ti K-α emission from the ionized material. The high fraction of Ti produced a bright fluorescence signal when exposed to probe radiation. The relative atomic fractions of $TiO_2/SiO_2 = 1.8$ in the foam were measured using Rutherford Backscattering Spectrometry (RBS), corresponding to a mass ratio of 2.4.

IV. MODELING MATERIAL COMPRESSION

Simultaneous density and K-α emission measurements of the shocked foam were made using the spatial and spectral IXS data. An overview of the data obtained from a single XRF measurement is shown in Fig. 3.

The XRF signal from an emitting region in the foam can be estimated by[26]

$$\gamma_{det} = N_p e^{-\alpha_p z_p}\left(1 - e^{-\alpha_{p,pe}\Delta z}\right) f_{K\alpha} e^{-\alpha_f z_f} \eta_{sys}, \quad (1)$$

where N_p is the number of probe x-rays incident on the sample, α is the photon attenuation coefficient, z is the length the x-rays must travel in the material, Δz is the length of the emitting region (defined by the spatial resolution of the detector), $f_{K\alpha}$ is the fraction of excited atoms decaying via K-α emission, and η_{sys} is a dimensionless factor to account for the geometry of the system including the source characteristics and detector solid angle. The subscripts p and f refer to the probe and fluorescence x-rays, respectively, and p, pe refers to only the photoelectric absorption term of the attenuation coefficient.

The x-ray attenuation coefficients were calculated using mass attenuation coefficients from the XCOM database,[18] μ, and the appropriate material densities, ρ, using $\alpha = \mu\rho$. α_p and α_f are loss terms and are calculated using the total attenuation of the foam for each energy. The term $\alpha_{p,pe} = \mu_{p,pe}\rho_d$ accounts for probe x-rays creating electron vacancies and is therefore calculated using only the photoelectric absorption coefficient of the probe x-rays by the fluorescing element and the density of that element. In this analysis we assume that the mass attenuation coefficients are constant.

A. Unshocked region

The initial density of the foam was measured using the spatial data from the IXS in the unshocked region from z = 1200–1700 μm, as illustrated in the inset of Fig. 2. The unshocked data were fit and ρ_0 was determined using the calculated XRF signal as a function of z, given by

$$\frac{I}{I_0} = \exp\left[-\mu\rho_0(L - z)\right]\left(\frac{R_s^2}{R_s^2 + (L + D - z)^2}\right), \quad (2)$$

where μ is the mass attenuation coefficient of the probe x-rays by the foam, R_s is the radius of the emitting region of the probe source, I_0 is a normalization factor, and dimensions L and D are defined in Fig. 2. The first term accounts for attenuation of the probe x-rays by the foam and the second term accounts for the distance from the probe source. This formula is strictly valid only on the

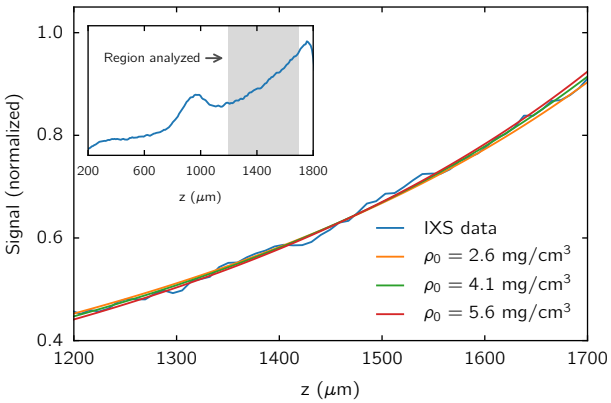

FIG. 4. Results of fitting Eq. 2 to the unshocked region of the spatially resolved data (illustrated in the inset), yielding an initial foam density of $\rho_0 = 4.1 \pm 1.5$ mg/cm^3.

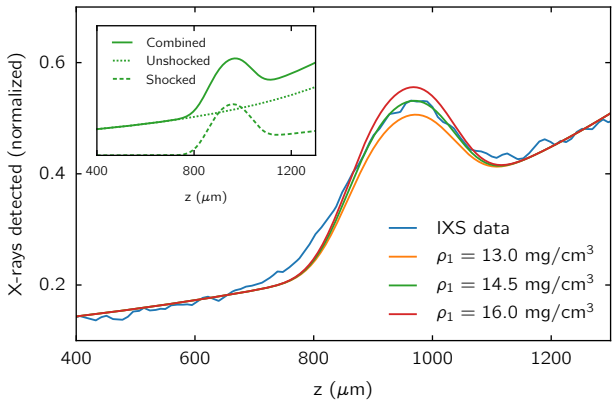

FIG. 5. Fits to the spatial data at the shock location at t = 15 ns. XRF signals from strong shock density profiles with contributions from unshocked material are plotted for $\rho_1 = 14.5 \pm 1.5$ mg/cm^3. The inset shows the XRF signal contributions from the two regions.

axis of the shock tube, but the experimental geometry makes this a reasonable approximation.

At the probe energy of 5.2 keV the total mass attenuation coefficient of the foam is $\mu_p = 322.0$ cm^2/g. The density of the unshocked foam was found to be $\rho_0 = 4.1 \pm 1.5$ mg/cm^3, where the error bars represent the maximum deviations from the best fit deemed plausible by the authors, as shown in Fig. 4. Knowing the mass ratio of the TiO_2 and SiO_2 from RBS measurements, we conclude that the foam used in this experiment consisted of 1.2 ± 0.4 mg/cm^3 SiO_2 and 2.9 ± 1.1 mg/cm^3 TiO_2.

B. Shocked region

The shock profile produced by the 600 μm drive beam was expected to be curved and only approximate a planar shock near the axis of the tube, with the width of the planar region decreasing as the shock propagates. The IXS provides an integrated measurement of all material in a spatial element (dz) along the axis of the shock tube. To calculate the XRF signal from this system a simple two region model was used, which consisted of a shocked inner region and an unshocked outer region. The density profile of the shocked aerogel was assumed to be a strong shock with no release rarefaction. This model was used because the mass of the 6 μm thick ablator was greater than the total mass of the shocked aerogel at the time it was probed. This suggests that the ablator density was still greater than the shocked aerogel density and acted as a piston compressing the foam.

The contributions to the XRF signal from each of the two regions is shown in the inset of Fig. 5. As predicted by the piston model, only the outer, unshocked region contributes to the signal well behind the shock front ($z < 700$ μm). This feature allowed the fraction of unshocked material to be determined and it was found that 74% of the signal came from the unshocked region.

The peak in the spatial data was fit by varying the width (in z) of the shocked region, post-shock density, and location of the shock. Bounds were set on the post-shock material density using this method. Fig. 5 shows the calculated spatial signal and the measured post-shock density of $\rho_1 = 14.5 \pm 1.5$ mg/cm^3. The slight disagreement between the fit and the IXS data in the region behind the shock is most likely a result of the simple two layer model not accounting for additional material on the edges of the curved shock front. This measurement could be significantly improved by selectively probing the planar shock region, which could be done with a collimator[5] or by probing with an x-ray free-electron laser.

The shock velocity in the Ti aerogel foam was 70 μm/ns, calculated by the shock location at t = 15 ns, resulting in 70 μm of motion blurring during the 1 ns duration of the probe. This effect was included in the modeling of the spatial information by integrating the calculated signal over this duration. This was done by calculating the density profile and resulting XRF signal at a number of time steps and integrating the signals. The total signal was then normalized to the intensity of the unshocked region.

V. INFERRING T_e FROM K-α SPECTRA

CRETIN[21] was used to calculate the K-α spectra for the density and temperatures expected in this experiment. CRETIN is a multi-species atomic kinetics and radiation code, which provided a self-consistent model for spectral emission of the heated region. Screened-hydrogenic atomic models[27] were used for Si and O, while more detailed atomic data for Ti were calculated using the Flexible Atomic Code (FAC).[28] The atomic model for Ti incorporated data describing all singly and dou-

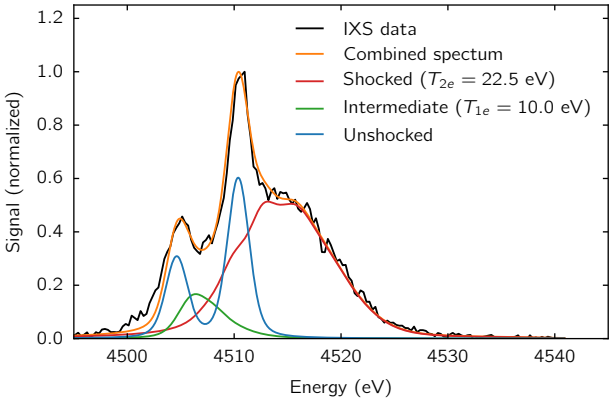

FIG. 6. Spectral fitting results for shock heated aerogel using spectra from CRETIN[21] simulations. Contributions from three regions were used to model the curved shock produced in this experiment. Although three regions are required to accurately model the full range of the IXS spectral data, the line shape in the range of 4515–4540 eV is dominated by the shocked region.

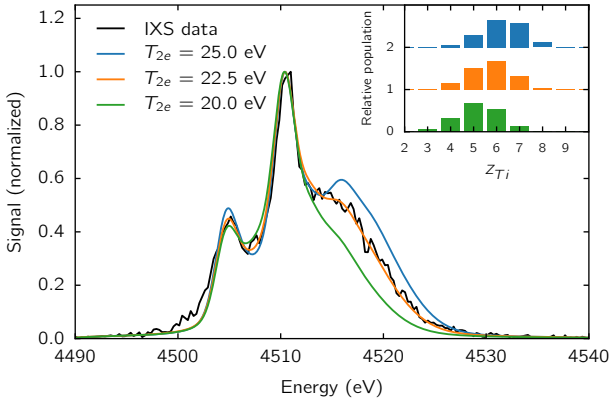

FIG. 7. Spectral fitting Ti K-α fluorescence from shock heated aerogel using CRETIN[21] used to infer an electron temperature in the post-shock material of $T_{2e} = 22.5 \pm 2.5$ eV. Bounds on electron temperature were set by fitting to measurements from the IXS and the relative ionization states of Ti present in each case are shown in the inset. The spectra for the upper and lower temperature bounds were calculated at the upper and lower bounds of material densities calculated using the spatial data from the IXS.

bly excited states within each ionization state up to a maximum principal quantum number of 8, averaged over configurations while maintaining a spectral resolution of 1 eV.

Calculations of XRF spectra were performed for a range of electron temperatures and material densities to fit the IXS spectral data in the heated region. In order to fit the spectra, contributions from the shocked and unshocked regions are included, as well as a small component from material at an intermediate temperature to account for edge effects in the curved shock. The addition of the intermediate component is required to properly fit the spectra in the 4500–4510 eV range, but has little effect on the spectra in the 4515–4540 eV range where the contribution from the hottest region dominates. These three regions are labeled 0, 1, and 2 for the unshocked, intermediate, and shocked regions, respectively. The spectral contributions from the three regions along with the combined fit to the IXS data are shown in Fig. 6, where the best fit for the electron temperature in the intermediate region was found to be $T_{1e} = 10.0$ eV. In reality, this intermediate region consists of material at a range of temperatures, but this simple model is reasonable considering the relatively small spectral contribution of this region.

For the conditions present in this experiment, the mean ionization state increases with decreasing density, requiring the lower and upper bounds on the electron temperature to be calculated at the lower and upper density bounds, respectively. Using this method, the post-shock electron temperature was found to be $T_{2e} = 22.5 \pm 2.5$ eV. Fig. 7 shows the results of the spectral fitting, with the relative ionization state populations present in each condition shown in the inset.

Improvements to this fit could be made by using more detailed atomic data for Ti and probing a more homogeneous region in the material. The 70 μm integration region, set by the spatial resolution of the IXS, and the curved shock front result in a measurement from a range of densities and temperatures. Here we have made an attempt to account for these effects with a three region model, but for high-precision EOS measurements a homogeneous region in the system should be probed.

VI. CONCLUSION

We have demonstrated the ability to use XRF to simultaneously measure ion density profiles, ionization-state distributions, and electron temperatures of shocked foams in the WDM regime. Fits to spatial data from an imaging x-ray spectrometer provided measurements of the initial and post-shock foam density. Spectral data were used to determine the Ti ionization-state distribution and electron temperature using K-α spectra calculated with CRETIN. XRF measurements provide a high-brightness diagnostic tool for WDM experiments. Combined with other diagnostic techniques, EOS measurements can improve our understanding of material properties in the WDM regime.

The high brightness and ability to selectively probe specific regions of a target using XRF make it a promising diagnostic for HED experiments in complex geometries. One example is the study of hydrodynamic instabilities in a diverging explosion.[29] Such an experiment could be diagnosed by exposing a thin layer of the target to probe radiation and placing the imaging diagnostic normal to the probed plane. 2D images with high signal-to-noise

could be obtained by using a spherical crystal x-ray optic, such as the Cu K-α spherical crystal imaging diagnostic currently at OMEGA.[30].

ACKNOWLEDGMENTS

The authors would like to thank the laser operations staff at the Trident Laser Facility for a successful experimental campaign, Robb Gillespie for machining the targets used in the experiments, and A. D. Loukianov for insightful discussions. This material is based upon work supported by the National Science Foundation Graduate Research Fellowship Program under Grant No. 2013155705. This work is funded by the NNSA-DS and SC-OFES Joint Program in High-Energy-Density Laboratory Plasmas, grant number DE-NA0001840 and by DTRA grant number DTRA-1-10-0077, and was supported by DOE Office of Science, Fusion Energy Science under FWP 100182. The portion of this work carried out at LLNL was performed under the auspices of the U.S. Department of Energy by Lawrence Livermore National Laboratory under contract DE-AC52-07NA27344.

* macdonm@umich.edu

[1] T. Guillot, Science **286**, 72 (1999).
[2] J. D. Lindl, P. Amendt, R. L. Berger, S. G. Glendinning, S. H. Glenzer, S. W. Haan, R. L. Kauffman, O. L. Landen, and L. J. Suter, Physics of Plasmas **11**, 339 (2004).
[3] D. Ryutov, R. P. Drake, J. Kane, E. Liang, B. A. Remington, and W. M. Wood-Vasey, The Astrophysical Journal **518**, 821 (1999).
[4] C. C. Kuranz, R. P. Drake, M. J. Grosskopf, A. Budde, C. Krauland, D. C. Marion, A. J. Visco, J. R. Ditmar, H. F. Robey, B. A. Remington, A. R. Miles, A. B. R. Cooper, C. Sorce, T. Plewa, N. C. Hearn, K. L. Killebrew, J. P. Knauer, D. Arnett, and T. Donajkowski, Physics of Plasmas **16**, 056310 (2009).
[5] E. Gamboa, P. Keiter, R. Drake, K. Falk, D. Montgomery, and J. Benage, High Energy Density Physics **11**, 75 (2014).
[6] M. D. Knudson and R. W. Lemke, Journal of Applied Physics **114**, 053510 (2013).
[7] K. Falk, C. A. McCoy, C. L. Fryer, C. W. Greeff, A. L. Hungerford, D. S. Montgomery, D. W. Schmidt, D. G. Sheppard, J. R. Williams, T. R. Boehly, and J. F. Benage, Phys. Rev. E **90**, 033107 (2014).
[8] P. Glatzel and U. Bergmann, Coordination Chemistry Reviews **249**, 65 (2005).
[9] L. J. Suter, O. L. Landen, and J. I. Koch, Review of Scientific Instruments **70**, 663 (1999).
[10] N. E. Lanier, C. W. Barnes, R. Perea, and W. Steckle, Review of Scientific Instruments **74**, 2169 (2003).
[11] L. C. Jarrott, M. S. Wei, C. McGuffey, A. A. Solodov, W. Theobald, B. Qiao, C. Stoeckl, R. Betti, H. Chen, J. Delettrez, T. Doppner, E. M. Giraldez, V. Y. Glebov, H. Habara, T. Iwawaki, M. H. Key, R. W. Luo, F. J. Marshall, H. S. McLean, C. Mileham, P. K. Patel, J. J. Santos, H. Sawada, R. B. Stephens, T. Yabuuchi, and F. N. Beg, Nat Phys **advance online publication**, (2016).
[12] D. J. Hoarty, C. C. Smith, E. L. Clark, J. M. Foster, S. G. Gales, G. Magelssen, J. Workman, W. M. Wood, S. Caldwell, R. Chrien, J. Sandoval, T. Sedillo, P. Walsh, B. Carpenter, S. Compton, and T. Perry, Review of Scientific Instruments **75**, 3655 (2004).
[13] G. Gregori, S. B. Hansen, R. Clarke, R. Heathcote, M. H. Key, J. King, R. I. Klein, N. Izumi, A. J. Mackinnon, S. J. Moon, H.-S. Park, J. Pasley, N. Patel, P. K. Patel, B. A. Remington, D. D. Ryutov, R. Shepherd, R. A. Snavely, S. C. Wilks, B. B. Zhang, and S. H. Glenzer, Contributions to Plasma Physics **45**, 284 (2005).
[14] S. Hansen, a. Faenov, T. Pikuz, K. Fournier, R. Shepherd, H. Chen, K. Widmann, S. Wilks, Y. Ping, H. Chung, a. Niles, J. Hunter, G. Dyer, and T. Ditmire, Physical Review E **72**, 036408 (2005).
[15] S. N. Chen, G. Gregori, P. K. Patel, H.-K. Chung, R. G. Evans, R. R. Freeman, E. Garcia Saiz, S. H. Glenzer, S. B. Hansen, F. Y. Khattak, J. A. King, A. J. Mackinnon, M. M. Notley, J. R. Pasley, D. Riley, R. B. Stephens, R. L. Weber, S. C. Wilks, and F. N. Beg, Physics of Plasmas **14**, 102701 (2007).
[16] P. Neumayer, H. Lee, D. Offerman, E. Shipton, A. Kemp, A. Kritcher, T. Döppner, C. Back, and S. Glenzer, High Energy Density Physics **5**, 244 (2009).
[17] U. Zastrau, A. Sengebusch, P. Audebert, E. Brambrink, R. Fäustlin, T. Kämpfer, E. Kroupp, R. Loetzsch, Y. Maron, H. Reinholz, G. Röpke, E. Stambulchik, I. Uschmann, and E. Förster, High Energy Density Physics **7**, 47 (2011).
[18] M. Berger, J. Hubbell, S. Seltzer, J. Chang, J. Coursey, R. Sukumar, D. Zucker, and K. Olsen, "XCOM: Photon cross sections database," (2012).
[19] S. H. Glenzer and R. Redmer, Rev. Mod. Phys. **81**, 1625 (2009).
[20] N. K. Moncur, R. P. Johnson, R. G. Watt, and R. B. Gibson, Applied Optics **34** (1995).
[21] H. A. Scott, Journal of Quantitative Spectroscopy and Radiative Transfer **71**, 689 (2001), radiative Properties of Hot Dense Matter.
[22] N. Broll, X-Ray Spectrometry **15**, 271 (1986).
[23] A. C. Thompson, D. T. Attwood, E. M. Gullikson, M. R. Howells, J. B. Kortright, A. L. Robinson, J. H. Underwood, K.-J. Kim, J. Kirz, I. Lindau, P. Pianetta, H. Winick, G. P. Williams, and J. H. Scofield, "X-ray data booklet," (2009).
[24] E. J. Gamboa, D. S. Montgomery, I. M. Hall, and R. P. Drake, Journal of Instrumentation **6**, P04004 (2011).
[25] M. M. Biener, J. Biener, Y. M. Wang, S. J. Shin, I. C. Tran, T. M. Willey, F. N. Pérez, J. F. Poco, S. a. Gammon, K. B. Fournier, A. W. van Buuren, J. H. Satcher, and A. V. Hamza, ACS applied materials & interfaces **5**, 13129 (2013).
[26] M. J. MacDonald, P. A. Keiter, D. S. Montgomery, M. M. Biener, J. R. Fein, K. B. Fournier, E. J. Gamboa, S. R. Klein, C. C. Kuranz, H. J. LeFevre, M. J.-E. Manuel, J. Streit, W. C. Wan, and R. P. Drake, Review of Scientific Instruments **85**, 11 (2014).

[27] H. Scott and S. Hansen, High Energy Density Physics **6**, 39 (2010).
[28] M. F. Gu, Canadian Journal of Physics **86**, 675 (2008).
[29] M. J. Grosskopf, R. P. Drake, C. C. Kuranz, A. R. Miles, J. F. Hansen, T. Plewa, N. Hearn, D. Arnett, and J. C. Wheeler, Astrophysics and Space Science **322**, 57 (2008).
[30] C. Stoeckl, G. Fiksel, D. Guy, C. Mileham, P. M. Nilson, T. C. Sangster, M. J. Shoup, and W. Theobald, Review of Scientific Instruments **83**, 033107 (2012).